Ultrahigh pressure isostructural electronic transitions in hydrogen

Cheng Ji[1,2], Bing Li[1,3], Wenjun Liu[4], Jesse S. Smith[2]†, Arnab Majumdar[5], Wei Luo[5], Rajeev Ahuja[5], Jinfu Shu[1], Junyue Wang[1], Stanislav Sinogeikin[2]§, Yue Meng[2]†, Vitali B. Prakapenka[6], Eran Greenberg[6], Ruqing Xu[4], Xianrong Huang[4], Wenge Yang[1], Guoyin Shen[2]†, Wendy L. Mao[7,8], Ho-Kwang Mao[1,*]

[1]Center for High Pressure Science and Technology Advanced Research, Beijing 100094, China; [2]High Pressure Collaborative Access Team, Geophysical Laboratory, Carnegie Institution of Washington, Argonne, IL 60439, USA; [3]Center for the Study of Matter at Extreme Conditions and Department of Mechanical and Materials Engineering, Florida International University, Miami, FL 33199, USA; [4]Advanced Photon Source, Argonne National Laboratory, Argonne, IL 60439, USA; [5]Condensed Matter Theory, Materials Theory Division, Department of Physics and Astronomy, Uppsala University, Uppsala, S-75120, Sweden; [6]Center for Advanced Radiation Sources, University of Chicago, Chicago, IL 60637, USA; [7]Department of Geological Sciences, Stanford University, Stanford, CA 94305, USA; [8]Stanford Institute for Materials and Energy Sciences, SLAC National Accelerator Laboratory, Menlo Park, CA 94025, USA; †Present address: X-ray Science Division, Argonne National Laboratory, IL 60439, USA; §Present address: DAC Tools LLC, Naperville, IL 60565, USA.

*maohk@hpstar.ac.cn

Understanding the high-pressure transitions leading hydrogen molecules to become a proposed molecular metallic solid and finally an atomic metal[1], which is predicted to show exotic new physics with the topology of two-component (electron and proton) superconducting, superfluid condensate[2,3], remains one of the great unresolved problems in condensed matter physics[4,5]. Measurements of the crystal structures of solid hydrogen, which provide crucial information towards understanding the metallization of hydrogen under compression, are missing for most of the high pressure phases due to the significant technical challenges. Here we present a single-crystal X-ray diffraction (SXRD) study of solid hydrogen up to 254 GPa which reveals the crystallographic nature of transitions from phases I to III and IV. Hydrogen molecules remain in the hexagonal close-packed (hcp) crystal lattice accompanied by a monotonic increase in anisotropy as shown by a drop of the *c/a* ratio from 1.63 to 1.53, with a substantial kink upon the transformation to phase IV. The pressure dependent shift of unit-cell volume also exhibits a slope change entering phase IV, suggesting a second-order isostructural phase transition. Our study

suggests that hydrogen may undergo a series of isostructural transitions due to the massive distortion of the hcp Brillouin zone prior to eventual band closure and metallization.

Seven high pressure solid phases of molecular hydrogen have been reported as a result of prodigious experimental efforts during the past four decades, namely phases I[6], II[7],II'(deuterium)[8], III[9], IV[10,11], IV'[12], and V[13], all based on optical changes such as peak broadening, peak splitting, and intensity changes in Raman and IR spectra. Phases III and IV show the greatest spectral changes among these phases and are the focus of experimental investigations and theoretical interpretations. At room temperature (RT), phase I is stable from 5 to 190 GPa with freely rotating hydrogen molecules forming the hcp crystal structure as determined by SXRD[14-16]. Phase II is a low-temperature (<130 K) phase with minor shift of Raman and IR vibrons, revealing quantum orientational ordering of the hydrogen molecules on the hcp lattice[17]. Phase III appears above 150 GPa (low-temperature) with major shifting, splitting, and intensification in Raman and IR vibron and rotons, which was interpreted as classical orientational ordering of the hydrogen molecules, with crystal structures remaining close to hcp[17]. Phase IV, discovered at RT above 220 GPa, exhibits two distinct vibrational modes with pressure-dependent broadening and a steep frequency drop of the first vibron[10], in contrast to the single vibrational mode of phases I, II, and III. Fundamental structural changes with novel alternating molecular and graphene-like layers were theoretically proposed for phase IV[18,19]. At higher pressures at RT, phases IV' (270 GPa)[12] and V (325 GPa)[13] were reported on the basis of relatively subtle modifications in Raman spectra compared to phase IV, and their structures were thought to be slight modifications[20] of the proposed structure of phase IV. Direct crystallographic information for the pivotal phase IV has been the focus of hydrogen research since its discovery[10], but no successful result has yet been published.

Diamond-anvil cell (DAC) coupled with synchrotron XRD is the only feasible method for crystal structural determination of hydrogen above 100 GPa. Extending XRD of hydrogen to 200 GPa poses several daunting challenges. X-ray scattering power is proportional to the square of the atomic number. With the atomic number one, hydrogen has the lowest possible scattering power which further diminishes at high pressures due to its extremely high compressibility that shifts XRD peaks to smaller *d*-spacings and its extremely strong Debye-Waller effect that defines the decrease of X-ray scattering power with increasing scattering momentum ($2\pi/d$). The hydrogen XRD signals are easily overshadowed by the strong background scattering from surrounding materials, such as Compton scattering from the diamond anvils and diffraction from the heavy metal gasket materials (due to the tail of focused X-ray beam), resulting in a poor signal/background ratio (S/B). The S/B problem was first tackled by growing single crystals of hydrogen, which concentrated the intensity from an XRD ring for polycrystalline hydrogen samples into an XRD spot without changing the background level, thus increasing the S/B and enabling the successful determination of the hcp structure of phase I[14,16]. Growing hydrogen single crystals within a helium (He) medium, which reduces fragmentation of hydrogen crystals under compression, has extended SXRD of hydrogen up to 119 GPa[15], which was the previous record for studies at RT. At 100 K, XRD of fragmented crystals of phase III up to 190 GPa has been reported[21] with a relatively big sample using an anvil culet size larger than 100 μm. The breakage rate of such large culets increases greatly with further pressure increase. Many experimental groups in ultrahigh-pressure hydrogen research have been working to push hydrogen XRD to higher pressures, but the obstacles are formidable. Hundreds of experiments during the past decade have ended in broken diamonds without publishable structural information.

We spent the past five years conducting more than a hundred experiments in search of a solution to this experimental challenge. We identified two key problems, namely, premature diamond failure caused by their exposure to X-rays in the presence of highly compressed hydrogen, and the low S/B ratio of submicron fragmented hydrogen crystals above megabar pressures. DAC has been used successfully in X-ray studies of materials to the limit of beveled diamond anvils up to approximately 400 GPa. Hydrogen studies have also reached this general pressure limit near 400 GPa in Raman spectroscopic studies but not in X-ray studies. After excessive failure of diamond anvils in XRD experiments above 180 GPa, a test was conducted by loading H_2 samples in DACs, compressing to 180-270 GPa, leaving them at constant pressure for three days, and subjecting the samples to occasional Raman studies with laser. The samples survived under laser exposure, and pressures remained unchanged. Then the samples were subjected to XRD studies using high brilliance synchrotron monochromatic x-ray with energy ranging from 20 to 35 keV, and all experiments failed due to diamond breakage within 1 to 20 hours of X-ray exposure, thus clearly demonstrating the detrimental effect of X-ray exposure to diamonds in contact with high-pressure hydrogen. Nevertheless, XRD at these pressures is possible if the experiments can be managed with minimal X-ray exposure and rapid data collection within several hours.

This SXRD study extends the pressure of single-crystal H_2 in He method[15] up to 160 GPa (phase I) beyond which the method becomes impractical due to the requirement of a much bigger sample chamber (~10 μm) for extra He and the diffusive nature of He (see Methods). Compressing small pure solid hydrogen samples (~ 5 μm) has been known to achieve multi-megabar pressures[10], but it produces fragmented submicron hydrogen crystals which reduce diffraction signal by more than three orders of magnitude in comparison to a single crystal. Three additional approaches were taken to reduce the background signals from gasket, diamond, and x-ray radiation outside the submicron sampling area to overcome the low S/B ratio problem of the submicron crystals. Through fabrication of a composite gasket with a metal girdle and a cubic boron nitride (cBN) or magnesium oxide (MgO) insert (originally developed for electrical conductivity measurements[11]) which consists of lighter elements and lower X-ray scattering power than the commonly used heavy-metal tungsten or rhenium (Re) gaskets, the small H_2 samples (~5 μm in diameter) could be sealed and compressed to the maximum pressure, and XRD patterns without background from a surrounding heavier metal could be collected (Extended Data Fig. 1). This sample preparation approach was combined with either one of the two following diagnostic improvements. 1) multi-channel collimator (MCC)[22] was used to select a segment along the incident X-ray beam by accepting the diffraction signal from the hydrogen sample while rejecting the background signals before and after the sample, thus reducing the Compton scatterings from diamond anvils by more than 80%. 2) to continue the SXRD method with fragmented H_2 crystallites, the submicron grain size was matched by focusing X-ray nano-beam[23] (FWHM≈300 nm) onto the crystallites that produced valuable SXRD signal and eliminated excess beam outside the crystallites. The strategy of multiple improvements finally paid off; we firstly extended the SXRD study of phase I to 190 GPa and fit the pressure-volume (P-V) data by a third order Vinet equation-of-state (EOS) that yields K_0=0.110(6) GPa and K_0'=7.36(7) by fixing[15] V_0=84.495 Å^3. Then we were able to measure SXRD spots of H_2 phases III and IV up to 254 GPa. Our SXRD data indicate that both phases III and IV remain in hcp as phase I.

Three successful SXRD experiments of H_2 phase III were conducted at 194 GPa, 210 GPa, and 212 GPa at RT using the monochromatic nano-focus X-ray probe. Fig. 1a shows the sample configuration and the phase III characteristic Raman spectrum of the 212 GPa experiment. SXRD data was obtained by rotating the DAC about the Ω-*axis* from -19° to 19° with data collection step size of 0.2°. The MgO gasket insert resulted in a relatively clean background in the XRD images from the 5 μm hydrogen area, as shown in Fig. 1b. The low XRD background, in great contrast to that from a heavy metal gasket, enabled a total of 26 weak diffraction spots of H_2 to stand out above the background (Fig. 1c). The spots are sharp with a good S/B ratio owing to the use of the nano-focus probe, which matches the grain size as illustrated in the Methods section. The 26 SXRD spots can be categorized into three families, (100), (002), and (101) of a hexagonal unit cell with *d*-spacings of 1.4978(6) Å, 1.356(1) Å, and 1.311(1) Å, respectively (Fig. 1d). The corresponding hcp unit cell parameters are a=1.7294(1) Å, c=2.7119(3) Å, and V=7.0245(8) Å^3. Due to the rapid decrease of the Debye-Waller factor at small *d*-spacing, the higher order reflections above (101) are extremely weak, below the present S/B detection limit The measured XRD spots are from different crystallites, as it is impractical to keep the nano-focused X-ray probe on the same submicron crystallite during the sample rotation of ±19°. The observation of the hcp lattice at RT is consistent with the previous powder XRD study of phase III, measured at 100 K up to 190 GPa that suggested the H_2 molecules remaining in the hcp sites[21].

The same strategy was applied for SXRD of H_2 phase IV at four pressures and RT, 220 GPa, 232 GPa, 244 GPa, and 254 GPa GPa. For the sample at 232 GPa, three sets of Ω-scans were conducted at three adjacent sample positions 1 μm apart (shown in Fig. 2a). A total of 40 sharp XRD spots were identified (Fig. 2b), with 20, 14, and 6 XRD spots (Fig. 2c) observed at each sample position (Extended Data Table 1 and Extended Data Fig. 2 provide detailed information of individual XRD spots). These reflections can be categorized into three d-spacing values of 1.4795(9) Å, 1.322(1) Å, and 1.2910(9) Å, and indexed as (100), (002), and (101), respectively, of a hexagonal lattice (Fig. 2d) with unit cell parameters of a=1.7084(1) Å, c=2.6431(2) Å, and V=6.681(1) Å^3. In addition, another three H_2 samples at 251 GPa, 251 GPa, and 244 GPa were measured by using a 2x1 μm^2 focused X-ray probe and with the use of MCC. Due to the larger X-ray beam, diamond failure occurred during exposure to the high brilliance synchrotron X-ray beam within 3 hours. One or two reflections, corresponding to (100), (002), or (101) could be recorded before diamond failure for each experiment and the results are plotted in Fig. 2e. The unit cell parameters of H_2 phase IV at 254 GPa are: a=1.6878(1) Å, c=2.5866(9) Å, and V=6.381(2) Å^3 which is a thirteen-fold compression from its initial V_0=84.495 Å^3 (a fitting value at ambient pressure from the literature[15]), and represents a record high densification reported in experimental measurements of solids. Again, phase IV is demonstrated to be consistent with the hcp structure within experimental uncertainty of $\Delta d/d = \pm 0.1\%$.

The hexagonal unit cell parameters of H_2 phases I, III, and IV at RT are plotted as functions of pressure in Fig. 3. The lattice parameter a decreases smoothly under compression (Fig. 3a), but an obvious kink in the pressure shift in c is observed across the phase boundaries (Fig. 3b), showing the collapse of c in phase IV. The unit cell volumes of phases III and IV follow the extrapolation of phase I without first-order discontinuity, but phase IV appears to be more compressible than phase I (Fig. 3c), revealing a second-order phase transition. The bulk modulus at 235 GPa, $K_{235} = -V_{235} \times (\frac{dP}{dV})_{235}$, of phase IV (461.5 GPa) is 14% smaller than that based on the EOS of phase I (536.8 GPa). The c/a ratio of hydrogen phase I at 5.4 GPa[14] is 1.630 which is close to the ideal value 1.633 for close-packed spheres. In previous XRD studies, hydrogen phase I has been reported to become anisotropic with increasing pressure, exhibiting a reduced c/a ratio[15,16,24]. Our measurements show that the c/a ratio keeps decreasing and the anisotropy continues to grow under further compression into phases III and IV (Fig. 3d). The transition to phase IV clearly marks a kink in the rate of the c/a ratio dropping which accelerates in phase IV and reaches 1.5325(5) at 254 GPa.

Phase IV of hydrogen was originally discovered based on changes of the Raman spectra. Raman optical spectra were collected along with XRD studies, and the results confirm previous observations in phase III and IV[10,11] (Extended Data Fig. 3), with a precipitous drop in Raman vibron frequency and an increase in vibron FWHM at the I-III transition. The trend of spectral changes continues and accelerates through the III-IV transition, with the emergence of an additional vibron peak v_2. The XRD measurements, which probe the mass centers of H_2 molecules and suggest the lattice being close to hcp, however, are insensitive to the intramolecular symmetry of the molecules. Combining the observations from both XRD and Raman, phase IV appears to be isostructural with phases I and III but possessing intramolecular symmetry breaking. The characteristics of two vibrational modes in Raman and intensified Infrared spectra could have several potential causes, namely, H_2 motif distortion[25], ortho-para state[26], change transfer, electron-phonon coupling, *etc*. The clarification of the exact structure of phase IV requires further theoretical investigations taking into account of the constraints provided by our XRD measurements.

Such high-pressure isostructural transitions with *c/a* anomaly and changes of optical and vibrational properties are not rare in hcp elements, such as Fe[27], Co[28], Os[29], Hf[30], *etc*., and invariably indicate electronic topological transitions (ETTs). Although these elements are atomic metals and high-pressure solid hydrogen is a molecular insulator on its way to an atomic metal, the theory of ETT would be a reasonable starting concept to consider. Since the XRD results suggest iso-structural phase transitions, we performed theoretical calculations of the electronic band structure using the hcp model ($P6_3/mmc$ and structure of phase I) as an approximation. Our preliminary theoretical calculations indicate that ETT may be a promising direction to account for phase transitions in hydrogen (See Extended Data for more details). A full treatment of the electronic nature of the isostructural transition, however, would be the goal of future comprehensive theoretical studies.

In summary, by overcoming a series of obstacles, the pressure range of SXRD studies on H_2 at RT was doubled to 254 GPa covering phases I, III, and IV. The SXRD data demonstrate that these high-pressure transitions in H_2 are not caused by major crystallographic changes of the hcp structure, remaining isostructural except for a severe distortion in the *c/a* ratio and an increase in anisotropy. Raman measurements confirm the previous observation of substantial peak broadening and frequency plummeting during the transitions. We identify the transition to phase IV phenomenologically as molecular symmetry-breaking isostructural transition of hydrogen, possibly with changes in its electronic structure. With a new generation of synchrotron nano-probes on the horizon, our work opens up opportunities for understanding the fascinating phase diagram of hydrogen by direct SXRD study to even higher pressure-temperature ranges.

References

1 Wigner, E. & Huntington, H. B. On the Possibility of a Metallic Modification of Hydrogen. *J Chem Phys* **3**, 764 (1935).

2 Babaev, E., Sudbø, A. & Ashcroft, N. W. A superconductor to superfluid phase transition in liquid metallic hydrogen. *Nature* **431**, 666-668 (2004).

3 Bonev, S. A., Schwegler, E., Ogitsu, T. & Galli, G. A quantum fluid of metallic hydrogen suggested by first-principles calculations. *Nature* **431**, 669-672 (2004).

4 McMahon, J. M., Morales, M. A., Pierleoni, C. & Ceperley, D. M. The properties of hydrogen and helium under extreme conditions. *Rev of Mod Phys* **84**, 1607-1653 (2012).

5 Mao, H.-k., Chen, X.-J., Ding, Y., Li, B. & Wang, L. Solids, liquids, and gases under high pressure. *Rev of Mod Phys* **90**, 15007 (2018).

6 Mao, H.-k. & Hemley, R. J. Ultrahigh-pressure transitions in solid hydrogen. *Rev of Mod Phys* **66**, 671-692 (1994).

7 Lorenzana, H. E., Silvera, I. F. & Goettel, K. A. Orientational phase transitions in hydrogen at megabar pressures. *Phys Rev Lett* **64**, 1939 (1990).

8 Liu, X. D., Howie, R. T., Zhang, H. C., Chen, X. J. & Gregoryanz, E. High-Pressure Behavior of Hydrogen and Deuterium at Low Temperatures. *Phys Rev Lett* **119**, 065301 (2017).

9 Hemley, R. J. & Mao, H. K. Phase transition in solid molecular hydrogen at ultrahigh pressures. *Phys. Rev. Lett.* **61**, 857-860 (1988).

10 Howie, R. T., Guillaume, C. L., Scheler, T., Goncharov, A. F. & Gregoryanz, E. Mixed molecular and atomic phase of dense hydrogen. *Phys Rev Lett* **108**, 125501 (2012).

11 Eremets, M. I. & Troyan, I. A. Conductive dense hydrogen. *Nat Mater* **10**, 927-931 (2011).

12 Howie, R. T., Scheler, T., Guillaume, C. L. & Gregoryanz, E. Proton tunneling in phase IV of hydrogen and deuterium. *Physical Review B* **86** (2012).

13 Dalladay-Simpson, P., Howie, R. T. & Gregoryanz, E. Evidence for a new phase of dense hydrogen above 325 gigapascals. *Nature* **529**, 63-67 (2016).

14 Hazen, R. M., Mao, H. K., Finger, L. W. & Hemley, R. J. Single-crystal x-ray diffraction of n-H_2 at high pressure. *Phys Rev B* **36**, 3944-3947 (1987).

15 Loubeyre, P. *et al.* X-ray diffraction and equation of state of hydrogen at megabar pressures. *Nature* **383**, 702-704 (1996).

16 Mao, H.-k. *et al.* Synchrotron X-ray Diffraction Measurements of Single-Crystal Hydrogen to 26.5 Gigapascals. *Science* **239**, 1131-1134 (1988).

17 Mazin, I. I., Hemley, R. J., Goncharov, A. F., Hanfland, M. & Mao, H.-k. Quantum and Classical Orientational Ordering in Solid Hydrogen. *Phys rev lett* **78**, 1066-1069 (1997).

18 Liu, H., Zhu, L., Cui, W. & Ma, Y. Room-temperature structures of solid hydrogen at high pressures. *J Chem Phys* **137**, 074501 (2012).

19 Pickard, C. J., Martinez-Canales, M. & Needs, R. J. Density functional theory study of phase IV of solid hydrogen. *Phys Rev B* **85**, 214114 (2012).

20 Monserrat, B. *et al.* Structure and Metallicity of Phase V of Hydrogen. *Phys Rev Lett* **120**, 255701 (2018).

21 Akahama, Y., Mizuki, Y., Nakano, S., Hirao, N. & Ohishi, Y. Raman scattering and X-ray diffraction studies on phase III of solid hydrogen. *J of Phys Conf Ser* **950**, 042060 (2017).

22 Prescher, C. *et al.* Beyond sixfold coordinated Si in SiO2 glass at ultrahigh pressures. *Proc Natl Acad Sci U S A* **114**, 10041-10046 (2017).

23 Wang, L. *et al.* Nanoprobe measurements of materials at megabar pressures. *Proc Natl Acad Sci U S A* **107**, 6140-6145 (2010).

24 Akahama, Y. *et al.* Evidence from x-ray diffraction of orientational ordering in phase III of solid hydrogen at pressures up to 183 GPa. *Phys Rev B* **82**, 060101 (2010).

25 Magdău, I. B., Marqués, M., Borgulya, B. & Ackland, G. J. Simple thermodynamic model for the hydrogen phase diagram. *Physical Review B* **95** (2017).

26 Goncharov, A. F., Eggert, J. H., Mazin, I. I., Hemley, R. J. & Mao, H.-k. Raman excitations and orientational ordering in deuterium at high pressure. *Phys Rev B* **54**, R15590-15593 (1996).

27 Glazyrin, K. *et al.* Importance of correlation effects in hcp iron revealed by a pressure-induced electronic topological transition. *Phys Rev Lett* **110**, 117206 (2013).

28 Kvashnin, Y. O., Sun, W., Marco, I. D. & Eriksson, O. Electronic topological transition and noncollinear magnetism in compressed hcp Co. *Phys Rev B* **92**, 134422 (2015).

29 Feng, Q., Ekholm, M., Tasnádi, F., Jönsson, H. J. M. & Abrikosov, I. A. Topological transitions of the Fermi surface of osmium under pressure: An LDA+DMFT study. *New J Phys* **19**, 033020 (2017).

30 Sun, W., Luo, W., Feng, Q. & Ahuja, R. Anisotropic distortion and Lifshitz transition in α-Hf under pressure. *Phys Rev B* **95**, 115130 (2017).

Figure Legends

Fig. 1 | Phase III sample and data. a. Micro-image of the hydrogen sample at 212 GPa and RT (phase III conditions), with illuminated in both transmitted and reflected light. Inset shows the measured Raman vibron. **b**. Merged raw XRD images showing the XRD spots. The color-code, with red, green, and blue representing (100), (002), and (101) reflections, respectively, is used throughout b, c, d. **c.** Montage of 26 XRD spots showing the data quality. **d**. Quality of indexing, showing *d*-spacing of (100), (002), and (101) reflections measured at different Ω angles. Dash lines show the calculated *d*-spacing values based on fitted unit cell parameters.

Fig. 2 | Phase IV sample and data. **a**. Micro-image of the H_2 sample at 232 GPa and RT (phase IV conditions) with illuminated in both transmitted and reflected light. Upper inset shows the magnified image on the sample area corresponding to the red dash box in the main image. Three blue dots mark the SXRD sampling positions. Lower inset shows the measured Raman vibrons. Blue arrow marks the characteristic new peak of phase IV. **b**. Merged raw XRD images showing the XRD spots. Red, green, and blue boxes mark (100), (002), and (101) reflections, respectively for b, c, d. **c.** Montage of 40 XRD spots showing the data quality. **d**. Quality of indexing, showing *d*-spacing of (100), (002), and (101) reflections measured at different **Ω** angles. Dash lines show the calculated *d*-spacing values based on fitted unit cell parameters. **e.** Comparison of *d*-spacing of reflections measured from the samples using the 2x1 μm^2 X-ray probe (HMO#18, #19, and #21) with that measured by using Nano-probe. HMO#19 and #21 were measured with MCC, and HMO#18 was measured without MCC. HMO and HBN represent the samples with MgO and cBN as insertion materials in the composite gaskets, respectively. Insets show diffraction spots from the three samples.

Fig. 3 | Unit cell parameters of H_2 under high pressures at RT. **a** and **b** show pressure dependent unit cell parameters *a* and *c*, respectively. Solid circles and solid triangles represent data collected by using MCC and nano-probe, respectively, with different colors marking different runs. Red squares represent data collected from H_2 crystals grown in He media. Black and blue lines are fitting of phases I and IV data, respectively. Legends in a and b also apply in c and d. **c.** Pressure dependent unit cell volume of H_2. Open blue squares are data from Loubeyre *et al*[15]. **d**. Evolution of *c/a* ratio with compression. In all figures, error bars represent standard deviations. Many error bars are smaller than the size of symbols. Calibrated pressure-dependent shift of d_{100} of H_2 was used as the pressure scale.

Acknowledgement

The authors thank R. Ferry and M. Somayazulu for helps with gas loading systems, Y. Wang for the use of the MCC of GeoSoilEnviroCARS (GSECARS), E. Gregoryanz, A. Goncharov, D. Kim, D. Popov, Y. Ma, H. Liu, and J. Tse for useful discussions. This research was supported by the Department of Energy (DOE), Office of Basic Energy Science, Division of Materials Sciences and Engineering under Award DE-FG02-99ER45775. Portions of this work were performed at 34 IDE, 16 IDB (HPCAT), 13 IDD (GSECARS), and 1-BM of Advanced Photon Source (APS), Argonne National Laboratory (ANL) in USA, as well as BL15U1, Shanghai Synchrotron Radiation Facility (SSRF) in China. HPCAT operations are supported by DOE, National Nuclear Security Administration under Award DE-NA0001974. VP is grateful to the NSF MRI EAR/IF1531583 award. GSECARS is supported by the National Science Foundation—Earth Sciences (Grant No. EAR-1128799) and DOE—Geosciences (Grant No.DE-FG02-94ER14466). This research used resources of the APS, a U.S. DOE Office of Science User Facility operated for the DOE Office of Science by ANL under Contract No. DE-AC02-06CH11357. A.M, R.A and W.L would like to acknowledge the support from Carl Tryggers Stiftelse for Vetenskaplig Forskning (CTS) and the Swedish Research Council (VR). SNIC and HPC2N are also acknowledged for providing computing time.

Author contributions

H.K.M. conceived and supervised the project; C.J., and B.L. conducted the synchrotron XRD measurements; W-J.L., R.X., J.S.S., S.S., Y.M., V.B.P., E.G., and G.S. developed techniques on synchrotron beamlines for H_2 XRD measurements; J.W., J.S., B.L., W.Y., X.H., and C.J. developed DAC related techniques to achieve the target ultrahigh pressure experimental conditions; C.J. conducted the Raman experiments; C.J. and J.S. prepared DAC samples; C.J., H.K.M., G.S., and W.Y., performed the analysis; H.K.M and W.L.M. conceived and developed the ETT interpretation. A.M., W.L., and R.A. conducted the *ab-initio* calculations. H.K.M. and C.J. wrote the manuscript in consultation with W.L.M., G.S., W.Y., V.B.P., E.G., B.L., W-J.L., J.S.S., A.M., W.L., R.A., and Y.M.

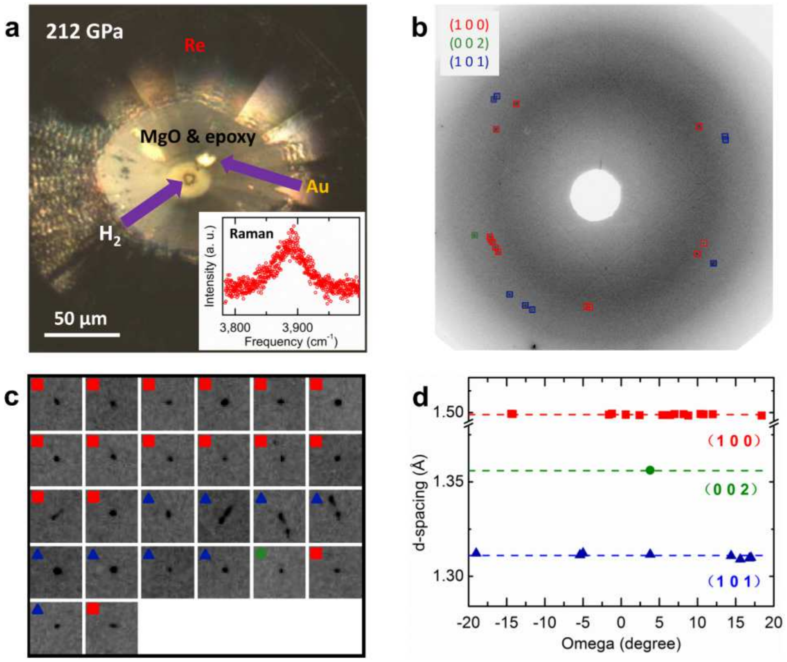
a
212 GPa
Re
MgO & epoxy
Au
H2
Raman
Intensity (a. u.)
3,800
3,900
Frequency (cm-1)
50 μm
b
(1 0 0)
(0 0 2)
(1 0 1)
c
d
1.50
1.35
1.30
d-spacing (Å)
(1 0 0)
(0 0 2)
(1 0 1)
-20
-15
-10
-5
0
5
10
15
20
Omega (degree)

Fig.1.

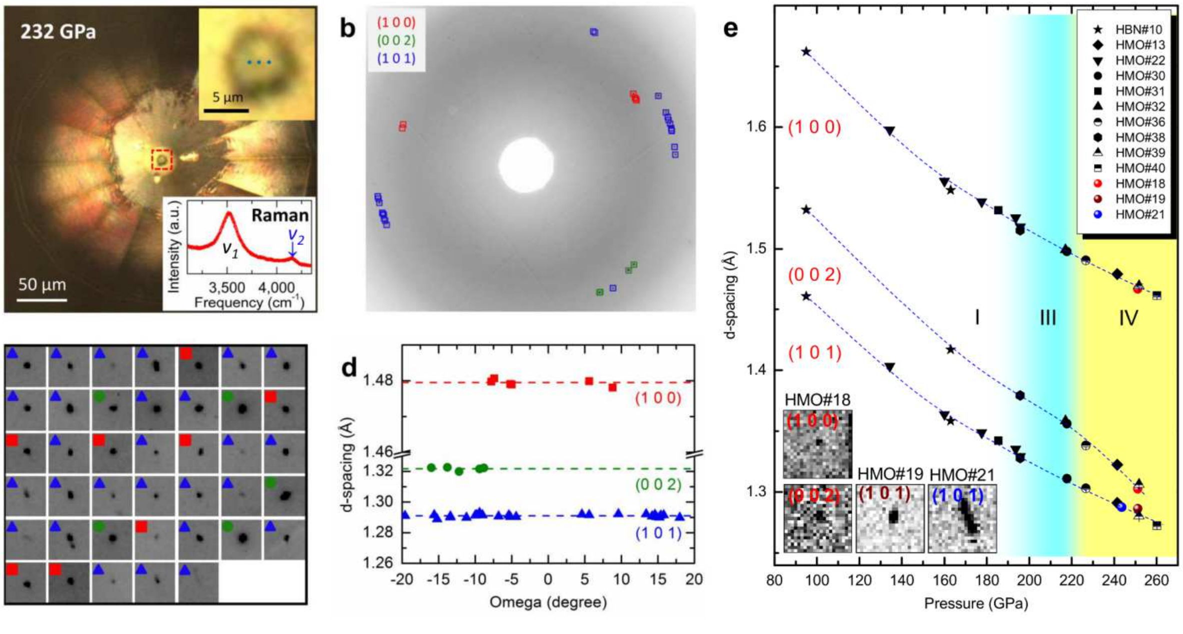
a
232 GPa
5 µm
50 µm
Raman
Intensity (a.u.)
v_1
v_2
3,500
4,000
Frequency (cm^{-1})
b
(1 0 0)
(0 0 2)
(1 0 1)
c
d
1.48
1.46
1.32
1.30
1.28
1.26
d-spacing (Å)
(1 0 0)
(0 0 2)
(1 0 1)
-20
-15
-10
-5
0
5
10
15
20
Omega (degree)
e
HBN#10
HMO#13
HMO#22
HMO#30
HMO#31
HMO#32
HMO#36
HMO#38
HMO#39
HMO#40
HMO#18
HMO#19
HMO#21
1.6
1.5
1.4
1.3
d-spacing (Å)
(1 0 0)
(0 0 2)
(1 0 1)
I
III
IV
HMO#18
(1 0 0)
(0 0 2)
HMO#19
(1 0 1)
HMO#21
(1 0 1)
80
100
120
140
160
180
200
220
240
260
Pressure (GPa)

Fig. 2.

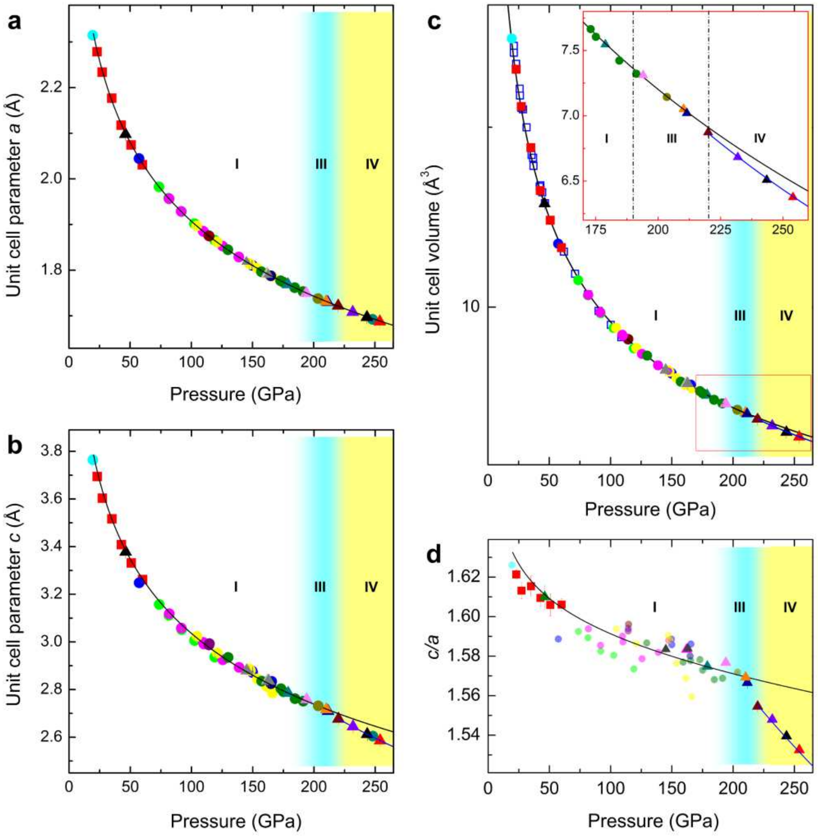
a
Unit cell parameter a (Å)
2.2
2.0
1.8
I
III
IV
0
50
100
150
200
250
Pressure (GPa)
b
Unit cell parameter c (Å)
3.8
3.6
3.4
3.2
3.0
2.8
2.6
I
III
IV
0
50
100
150
200
250
Pressure (GPa)
c
Unit cell volume (Å³)
10
I
III
IV
7.5
7.0
6.5
175
200
225
250
0
50
100
150
200
250
Pressure (GPa)
d
c/a
1.62
1.60
1.58
1.56
1.54
I
III
IV
0
50
100
150
200
250
Pressure (GPa)

Fig.3.

Methods

Symmetric DACs were used to generate ultrahigh pressures. Diamond anvils with culet size ranging from 150 μm down to 20 μm (anvils with culet sizes of 30 to 20 μm were used to achieve target pressures of phases III and IV) were used with more than a total of 100 samples prepared during the entire study. No surface coating was applied to the tips of diamond anvils. Two sample preparation strategies were used. The first type of samples had H_2 single crystal grown in the He pressure media, similar to the method reported by Loubeyre *et al*[15]. Premixed normal H_2 and He gas of 99.9% purity with 1:4 volume ratio was purchased from Airgas Inc. This type of samples is referred as H_2-He samples. H_2-He samples had sample chambers (laser drilled in pre-indented rhenium (Re) or tungsten (W) gaskets) relatively large in diameter (15 to 20 μm at megabar pressures) to allow growing H_2 single crystals with reasonable size (5 to 10 μm in diameter) for the XRD measurements. There is enough room in such a H_2-He sample chamber for loading a thin gold (Au) flake as the pressure marker[31]. The inset of Extended Data Fig. 5a shows the typical sample configuration of the H_2-He sample. We didn't observe any obvious difference of Raman spectra of the H_2-He samples comparing to pure H_2 samples at megabar pressures, as shown in Extended Data Figs. 5b and c. Immiscibility of solid H_2 and solid He was also reported up to 110 GPa and 250 GPa by Loubeyre *et al*[15] and Turnbull *et al*[32], respectively. Thus the pressure-dependent shift of the (100) *d*-spacing (d_{100}-P) measured from the H_2-He samples was used as the pressure scale (Extended Data Fig. 5a) for the samples in which no Au pressure marker was loaded. Since the H_2-He samples typically have strong preferred orientations so that almost only the (100) class can be measured. As a result, the measurements of H_2-He samples mainly serve to provide the d_{100}-P pressure scale. The XRD measurements of the H_2-He samples were performed at 16IDB of APS, ANL, with 6 μm by 7 μm focused monochromatic beam at 30 keV; at 13 IDD of APS, ANL, with 3 μm by 2 μm focused monochromatic beam at 37 keV; at BL15U1 of SSRF, with 2 μm by 2 μm focused monochromatic beam at 20 keV. These data were recorded by either Mar165 CCD detectors or a Pilatus 1M detector. The H_2-He samples require a relatively large sample chamber (~15 μm) for growing hydrogen single crystal (~5 μm). The larger the sample chamber the more exposure of the diamond anvil surface to the highly diffusive hydrogen or He, thus increasing the probability of premature diamond anvil failures which limited our measurements using H_2-He samples to below 160 GPa.

The second type of samples had pure H_2 loaded with composite gaskets in order to achieve clean XRD background on small samples. The application of the second sample preparation method with pure H_2 samples allowing small sample chamber (~5 μm in diameter) is to counter the premature diamond anvil failure problem which we have suffered by using the H_2-He single crystal method. The composite gaskets are the key to achieve clean XRD background. It has Re outskirt and MgO+epoxy or cBN+epoxy as inserts. The epoxy used is totally amorphous, pre-examined by XRD measurements. Sample chambers were fabricated using the laser micro-fabrication system[33] located at HPCAT, APS, ANL. All samples were loaded by sealing high pressure normal H_2 gas, of 99.99% purity commercially obtained (Airgas Inc.), at 0.16 GPa to 0.2 GPa using gas loading systems. No Au pressure marker was loaded inside the sample chambers to avoid strong diffraction of Au which may interfere with the identification of hydrogen XRD peaks. As mentioned above, the pressure scale derived from the H_2-He samples was used for the pressure determination of all pure-H_2 samples. Diamond Raman edge[34] and the equation of state of MgO[35] were also measured to cross-check pressures. For instance, pressure values obtained by Diamond Raman edge, d_{100}-P, and MgO pressure scales, for one of the phase IV samples measured using nano-focus probe, are 234 GPa, 232 GPa, and 238 GPa, respectively. The largest difference between these numbers is approximately 2.5% of the mean value, which is reasonable at the two-megabar pressure range.

The sample positions of the X-ray transparent small H_2 samples were determined by performing 2D diffraction contrast imaging based on XRD intensity of the insert gasket materials (MgO or cBN) as demonstrated in Extended Data Figs. 6a and b. XRD of pure-H_2 samples were measured using the nano-focus probe (34 IDE of APS, ANL) or 1 μm by 2 μm probe with MCC (16 IDB of APS, ANL). At 34IDE, X-ray probe was typically focused down to 300 nm in FWHM at 24 keV. The data using nano-focus probe was collected by rotational step scans typically of 0.2° step size within a ±19° angular range about the Ω-*axis,* and recorded using a Mar165 CCD detector. Typical data collection time for each angle ranges from 60s to 120s. At 16 IDB, 2x1 μm^2 focused monochromatic beam at 30 to 35 keV was used. Two types of MCC were used, with 10° and 30° vertical opening angles (4-theta), respectively. The MCC with 30° vertical opening angle was especially developed by HPCAT to facilitate the SXRD data collection of H_2 in phase IV conditions, as shown in Extended Data Fig. 7. A Pilatus 1M detector was used in the experiments with MCC. The data collection by MCC was performed by scanning the MCC by an angle range of typically 4°. Our data collection time for one frame ranges from 5 min to 20 min, depending on the data quality. Most of the *P-V* data of phase I was measured using the pure-H_2 samples with the use of the 10° MCC.

The Raman measurements were conducted using the con-focal micro-Raman system at HPSynC and GSECARS, located at the APS, ANL. Both systems are equipped with red excitation lasers, 659.5 nm, with the backscattering geometry and CCD camera. Dioptas[36] was used for XRD data reduction. XDI was used to perform the 2D XRD contrast imaging data analysis[37]. Fityk[38] was used to perform peak fitting to subtract the peak positions from the reduced XRD data. EoSFit7-GUI[39] was used for fitting the EOS.

The theoretical calculations of structural optimizations and total energy computations were performed using VASP[40] by solving the Kohn-Sham equations within the Density Functional Theory (DFT) framework[41]. The projector augmented wave (PAW) method[42], and the generalized gradient approximation (GGA) with the Perdew-Burke-Ernzerhof parametrization (PBE)[43] have been used to describe the electronic exchange-correlation effects. A dense Monkhorst-Pack[44] k-point mesh (30 x 30 x 20) was used for the Brillouin zone integration for the optimization of the structures, keeping a cut-off energy of 700 eV. For accurate electronic properties calculations, the GW approximation (implemented in VASP) was employed interfaced with the Wannier90 code[45].

Submicron hydrogen crystallites above megabar pressures

For the phase IV sample measured at 232 GPa using nano-focus probe, XRD patterns collected at the same Ω angle but at different spatial positions (1 μm apart) do not show the same XRD spot. This suggests that the size of crystal grains is submicron. However, since the samples above 210 GPa experienced diamond anvil failures during SXRD data collections, subsequent 2D XRD contrast imaging (tracking an selected H_2 XRD spot) was unable to be performed to exactly map out the grain size of the phase III or the phase IV samples. Fortunately, such an analysis was able to be performed on two hydrogen samples in phase I up to 163 GPa. The (100), (002), and (101) reflections were observed with spotty peak profiles similar to that obtained from the samples in phases III and IV. The size of the grains, resolved by the 2D contrast imaging analyses, is typically below one micron (Extended Data Figs. 6c to h). It is technically challenging to lock on a particular submicron crystal grain using the nano-focus probe while performing SXRD data collection by the rotating the DAC with a wide angle range.

XRD diagnostic strategies

The effects of using MCC and nano-focus probe, respectively, for measuring XRD of hydrogen at megabar pressures are briefly discussed as the following. The use of MCC with DAC in general improves the S/B ratio by cutting out the majority of the Compton scattering background from the thick diamond anvils. The thickness of a typical hydrogen sample above 200 GPa is tiny, approximately 1 μm, compared to the 4.8 mm total thickness of two diamond anvils. Our measurements show the background reduction being achieved by ~80% (Extended Data Figs. 8 a to c). However, data collection time is significantly increased due to the limited throughput of MCC. MCC with large vertical opening angle is especially beneficial for the SXRD data collection of hydrogen (Extended Data Fig. 7). Above multi-megabar pressures, H_2 crystals break down to submicron level (Extended Data Figs. 6c to h). Using a nano-focus X-ray probe to match the grain size significantly improves the S/B ratio. For example, if the grain size is 500 nm, using the 500 nm X-ray probe improves the S/B ratio by approximately a factor of 16 compared to that using a 2 um by 2 um X-ray probe with the same total flux (Extended Data Figs. 8d to f). A combination of nano-focus probe with the MCC could achieve even better S/B ratio. Since the use of MCC significantly increases the sample to detector distance (by a factor of 3 in our case), combining the nano-focus probe techniques with MCC requires a nano-focus beamline to be capable to deliver high flux photons with relatively high energy (>30 keV) or be equipped with a large area detector, such as the Pilatus 6M detector. Such developments are to be conducted to further facilitate the XRD measurements of solid hydrogen at ultrahigh pressures.

Electronic band structure calculations

Theoretical *ab initio* calculations were performed to check for ETT. Electronic band structures were calculated for various pressures, spanning all the three phases (I, III and IV). We utilized the hcp ($P6_3/mmc$) model, which is dynamically stable, for all the three phases studied. In agreement with earlier experimental observations on solid hydrogen[46], the electronic band gaps at 50 GPa and 100 GPa were calculated to be 4.3 eV and 3.8 eV, respectively (Extended Data Figs. 9a and b). The conduction band minimum (CBM) occurs at the Γ point while the valence band maximum (VBM) is found to occur from the Γ→A and Γ→K high symmetry directions, thus rendering phase I to be an indirect band gap semiconductor. However, a remarkable feature is obtained at higher pressures. With further compressions, the band gap keeps decreasing but the nature of the dispersion curves change drastically both in the valence and conduction regions in the vicinity of the Fermi level. At the same position of the VBM (Γ → A and Γ→ K) for phase I, there now appear Dirac-like cones (Extended Data Figs. 9c-e). The conduction band close to Fermi level is mainly of *s*-character (80%) with mixture of p-character (20%). It is also noticed from electronic structure that unoccupied *p* states are moving faster than *s* states towards the Fermi level. There are several immediate inferences which can be drawn. Due to the appearance of the Dirac-like cones in close proximity to the Fermi level, the density of states on either side of the Fermi level changes. This is a requirement for non-degenerate semiconductors to undergo ETT. The CBM and VBM (belonging to the Dirac-like cones) manifest in the lower effective mass. The hcp phase now becomes a direct bandgap semiconductor. It would be interesting to further study how the Lifshitz transition would renormalize the bands and redistribute the electronic density of states. Although the metallization and superconductivity of hydrogen is predicted to happen at higher pressures, our findings pave the way for future studies to explore how the Dirac-like cones will affect the metallic and superconducting phases.

Admittedly, simple H_2 molecules at hcp lattice sites do not explain multiple Raman vibrons and intense IR spectra of phase IV and have a higher energy by DFT calculations in comparison to other candidate models, namely $C2/c$[47], $P6_122$[48], Pc[19], Cc[18], $Pca2_1$[20], *etc*. (Extended Data Fig. 10). The problems of intramolecular symmetry breaking and tens of meV higher energy can be easily accounted for by molecular level phenomena, such as: H_2 motif distortion[25], ortho-para state[26], change transfer, electron-phonon coupling *etc*. We used hcp as an approximation to explore changes of electronic band structure for the iso-structural phase transitions from phases I to III to IV.

References

31 Anderson, O. L., Isaak, D. G. & Yamamoto, S. Anharmonicity and the equation of state for gold. *J Appl Phys* **65**, 1534 (1989).

32 Turnbull, R. *et al.* Reactivity of Hydrogen-Helium and Hydrogen-Nitrogen Mixtures at High Pressures. *Phys Rev Lett* **121**, 195702 (2018).

33 Hrubiak, R., Sinogeikin, S., Rod, E. & Shen, G. The laser micro-machining system for diamond anvil cell experiments and general precision machining applications at the High Pressure Collaborative Access Team. *Rev Sci Instrum* **86**, 072202 (2015).

34 Akahama, Y. & Kawamura, H. Pressure calibration of diamond anvil Raman gauge to 410 GPa. *J Phys Conf Ser* **215**, 012195 (2010).

35 Speziale, S., Zha, C.-S., Duffy, T. S., Hemley, R. J. & Mao, H.-k. Quasi-hydrostatic compression of magnesium oxide to 52 GPa: Implications for the pressure-volume-temperature equation of state. *J Geophys Res* **106**, 515-528 (2001).

36 Prescher, C. & Prakapenka, V. B. DIOPTAS: a program for reduction of two-dimensional X-ray diffraction data and data exploration. *High Pressure Res* **35**, 223-230 (2015).

37 Hrubiak, R., Smith, J. S. & Shen, G. Multimode scanning X-ray diffraction microscopy for diamond anvil cell experiments. *Rev Sci Instrum* **90**, 025109 (2019).

38 Wojdyr, M. Fityk: a general-purpose peak fitting program. *J Appl Crystallogr* **43**, 1126-1128 (2010).

39 Gonzalez-Platas, J., Alvaro, M., Nestola, F. & Angel, R. EosFit7-GUI: a new graphical user interface for equation of state calculations, analyses and teaching. *J of Appl Crystallogr* **49**, 1377-1382 (2016).

40 Kresse, G. & Hafner, J. Ab initio molecular dynamics for liquid metals. *Phys Rev B* **47**, 558(R) (1993).

41 Kohn, W. & Sham, L. J. Self-Consistent Equations Including Exchange and Correlation Effects. *Phys Rev* **140**, A1133 (1965).

42 Blöchl, P. E. Projector augmented-wave method. *Phys Rev B* **50**, 17953 (1994).

43 Perdew, J. P., Burke, K. & Ernzerhof, M. Generalized gradient approximation made simple. *Phys Rev Lett* **77**, 3865 (1996).

44 Monkhorst, H. J. & Pack, J. D. Special points for Brillouin-zone integrations. *Phys Rev B* **13**, 5188 (1976).

45 Mostofi, A. A. *et al.* An updated version of wannier90: A tool for obtaining maximally-localised Wannier functions. *Comput Phys Commun* **185**, 2309-2310 (2014).

46 Goncharov, A. F., Gregoryanz, E., Hemley, R. J. & Mao, H.-k. Spectroscopic studies of the vibrational and electronic properties of solid hydrogen to 285 GPa. *Proc Natl Acad Sci U S A* **98**, 14234-14237 (2001).

47 Pickard, C. J. & Needs, R. J. Structure of phase III of solid hydrogen. *Nat Phys* **3**, 473-476 (2007).

48 Monserrat, B., Needs, R. J., Gregoryanz, E. & Pickard, C. J. Hexagonal structure of phase III of solid hydrogen. *Physical Review B* **94** (2016).

Data Availability Statement

The data that support the findings of this study are available from the corresponding author upon request.

Extended Data legends

Extended Data Table 1 | Detailed information of the 40 reflections of the sample measured at 232 GPa using the nano-focus probe. Position # represents the sample position where the XRD data was measured. *Ω* angle represents the rotation angle of the sample about the *Ω-axis*. χ angle represents the azimuth angle of a diffraction spot on the CCD detector. Definition of the χ angle is illustrated in Extended Data Fig. 3. Only a few reflections were captured at the #3 sample position because the pre-mature failure of diamond anvil occurred during the early stage of the step scans at that sample position.

Extended Data Fig. 1 | Comparison of the XRD raw images obtained by using a pure Re gasket versus a composite gasket at the same beamline. **a.** XRD image at 45 GPa by using Re gasket. Inset shows the microscope image of the sample after gas loading, with the chamber diameter being 17 μm. At 45 GPa, the chamber shrunk with diameter being approximately 10 μm. **b.** Raw XRD of the sample at 162 GPa using insertion gasket (cBN+epoxy). Chamber diameter is 7 μm at 162 GPa. Setups of the beamline focusing device (Kirkpatrick-Baez (KB) mirrors) were similar for both a and b. Clean-up pinholes were used, with 20 μm for a and 60 μm for b, respectively. It needs to be emphasized that even though the X-ray probe used in b has larger tail (due to larger size of clean-up pinhole), b shows significantly cleaner background. MgO+epoxy insert produces similar level of clean background compared to that from the cBN+epoxy insert. Red masks in both a and b cover the gaps between the sensor chips on the Pilatus 1M detector.

Extended Data Fig. 2 | Definition of χ angle in the XRD image. Blue arrow points to a diffraction spot, which is inside the red circle.

Extended Data Fig. 3 | Features of Raman vibrons of hydrogen under high pressures. **a**. Pressure dependent frequency shift of vibrational modes of H_2 at RT. **b**. Pressure dependent shift of the widths (FWHM) of H_2 vibrational modes at RT. v_1 and v_2 represent the two fundamental vibrational modes of H_2, as shown in Extended Data Fig. 4. Solid circles and triangles represent v_1 and v_2 modes, respectively. Different colors represent different runs. Dash lines are visual guides. In phase III, the frequency of v_1 significantly softens with pressure compared to that in phase I. While, the Raman peak significantly broadens simultaneously. In phase IV, the behavior of v_1 is similar to that in phase III, while a new fundamental vibrational mode v_2 appear at higher frequency. Phase IV also exhibits new low frequency modes, as shown in Extended Data Fig. 4.

Extended Data Fig. 4 | Complete Raman spectrum corresponding to the Raman spectrum in the inset of Fig.2a (phase IV). It clearly shows the characteristic Raman features of phase IV, marked by blue triangles, the low frequency mode at 303 cm^{-1} and the second vibron at 4149 cm^{-1}. Inset shows the Diamond Raman edge with pressure determined to be 234 GPa, which shows a 2 GPa difference compared to our d_{100}-P scale.

Extended Data Fig. 5 | XRD measurements for the d_{100}-P pressure scale and immiscibility of H_2 and He indicated by Raman measurements. **a**. Evolution of *d*-spacing of the (100) reflection of H_2 measured in the H_2-He samples with Au as the pressure marker. The (111) reflection of Au standard was used to calculate pressure[31]. Inset shows the sample configuration. **b**. Raman spectra of the H_2-He samples at selected pressures. Different colors mark different runs. **c**. Comparison of the pressure-dependent shift of vibron frequency between the H_2-He samples and the pure H_2 samples. Open symbols represent pure hydrogen samples. Solid symbols represent H_2-He samples. Samples with names starting with HP and HX including H27 are pure H_2 samples. Other samples with names starting with H are H_2-He samples.

Extended Data Fig. 6 | 2D diffraction contrast imaging of MgO and H_2 (submicron crystallites). **a.** 2D diffraction contrast imaging based on the intensity of MgO (200) Bragg peak. Darker color represents higher intensity of MgO (200) peak. White area represents hydrogen sample. **b.** Micro-image of the same sample area with illuminated in both transmitted and reflected light. **c-h.** 2D diffraction contrast imaging based on intensities of selected XRD spots of H_2 samples at 97 GPa (**c**, **d**, and **e**), 163 GPa (**f** and **g**), and 162 GPa (**h**). Darker color represents higher peak intensity. Step size of the two-dimensional scan is 500 nm in both the horizontal and the vertical directions. Data analysis was performed using the XDI software[37].

Extended Data Fig. 7 | XRD raw images obtained by using MCCs with two different vertical opening angles of 10° (a) and 30° (b) in 4-theta, respectively. Data was collected using Pilatus 1M area detector. MCC with 10° vertical opening was obtained from GSECARS, APS, ANL. It is mainly designed for Large Volume Press, and for DAC in the studies of amorphous samples or powder samples. With 10° MCC in place, approximately only one third of the area detector can be exposed by X-ray (enclosed area inside the red box in a). This limited vertical opening isn't a problem in the study of amorphous or powder sample, because the X-ray scattering or diffraction is uniformly distributed about the X-ray beam thus can be captured by the area detector through the small window. However, for SXRD data collection, XRD spots show up at particular azimuth angles on the area detector. The limited vertical opening becomes an issue. As a result, the data collection using the MCC with 10° vertical opening was not trivial. It consists of the following steps: 1) Identify XRD spots without the MCC at low pressure; 2) rotate the sample about the χ-axis to move the target XRD spot into the MCC opening; 3) increasing pressure and track the XRD spot with the MCC. It would be extremely time consuming for directly searching a diffraction spot of hydrogen at above megabar pressure with the 10° MCC. Meanwhile, using the 10° MCC also indirectly result in the measurements of scattered *c/a* ratio, as can be noticed in MCC data of Fig. 3d. Most of these data above 100 GPa was measured using MCC with 10° vertical opening. Since searching for XRD spot using the MCC with 10° vertical opening is difficult, as explained above, and data collection with MCC takes extended exposure time, usually one (100) peak and one (101) peak were measured to determine the *c/a* ratio. These peaks are from different crystals with different crystal orientations, sustaining different stress conditions, resulting in the scattering *c/a* among different samples. MCC with 30° vertical opening was then designed especially by HPCAT to overcome the above problems. By using the 30° vertical opening MCC, almost the whole area detector can be exposed (enclosed area inside the red box in b). This significantly facilitates the SXRD data collection of H_2 at multi-megabar pressures. It is also suitable for performing SXRD study of other low Z materials in DAC at very high pressures.

Extended Data Fig. 8 | Demonstration of the effects of using MCC and submicron probe, respectively, for measuring XRD of solid hydrogen at megabar pressures. a. Comparison of the integrated hydrogen (100) peak with and without MCC at 143 GPa. With MCC, the background of data was reduced by a factor of 5. **b** and **c** show the corresponding raw images of the (100) peak. Integrations were performed using the same region of interest, which contains the target peak (as shown in b and c), and the same setups in Dioptas[36]. Data collection times with and without MCC are equivalent (the exposure with MCC is actually several times longer due to the limited throughput of MCC). Data was collected by using 2x1 μm^2 focused X-ray probe at 16IDB of APS. **d**, **e**, and **f** show the XRD images which correspond to equivalent beam size of 300 nm (real), 1 μm and 2 μm, respectively. Data was collected using 300 nm nano-focus probe. Data in d was collected at a single sample position with 60s exposure. Image in e was obtained by merging 9 images measured by a 3 by 3 two-dimensional scan with the same exposure time for each image (60s). Image in f was obtained by merging 49 images collected by a 7 by 7 two-dimensional scan with the same exposure time for each image (60s). Step size in these 2D scans was 500 nm. Red dots represent X-ray probe. It is obvious that a larger beam size which includes more background deteriorates the data quality.

Extended Data Fig. 9 | Electronic band structures calculated at 50 GPa (a), 100 GPa (b), 156 GPa (c), 193 GPa (d) and 240 GPa (e).

Extended Data Fig. 10 | Enthalpy difference of various phases of hydrogen as a function of pressure based on DFT calculation.

Extended Data Table 1

Peak #	Position #	Ω (°)	χ (°)	*d*-spacing (Å)
1	1	-15.6	28.0	1.2915
2	1	-9.4	305.0	1.2929
3	1	-9	18.0	1.2915
4	1	-8.8	314.1	1.3223
5	1	-7.8	34.0	1.4798
6	1	-7.4	31.8	1.4807
7	1	-7.4	32.1	1.4807
8	1	-6.8	7.4	1.2907
9	1	-5.2	31.4	1.4791
10	1	-5.2	14.4	1.2904
11	1	-4.4	13.8	1.2904
12	1	5.6	161.9	1.4799
13	1	5.6	199.3	1.2916
14	1	13.4	202.4	1.2921
15	1	14.6	199.7	1.2918
16	1	14.6	200.4	1.2909
17	1	14.8	191.7	1.2903
18	1	15.2	198.1	1.2900
19	1	15.4	201.0	1.2913
20	1	18	192.4	1.2899
21	2	-19.6	4.2	1.2910
22	2	-10	19.0	1.2913
23	2	-9.8	16.4	1.2915
24	2	-9	18.0	1.2915
25	2	-5.4	7.2	1.2914
26	2	-5	32.2	1.4790
27	2	-5	32.3	1.4789
28	2	4.6	201.3	1.2919
29	2	9.6	203.0	1.2922
30	2	14.2	200.3	1.2907
31	2	15.8	194.2	1.2915
32	2	-12.2	317.2	1.3199
33	2	8.8	163.2	1.4781
34	2	-9.4	299.7	1.3216
35	3	-16	300.0	1.3224
36	3	-15.2	63.2	1.2888
37	3	-13.8	300.0	1.3227
38	3	-13.4	63.6	1.2901
39	3	-13.4	16.4	1.2907
40	3	-11.2	21.1	1.2899

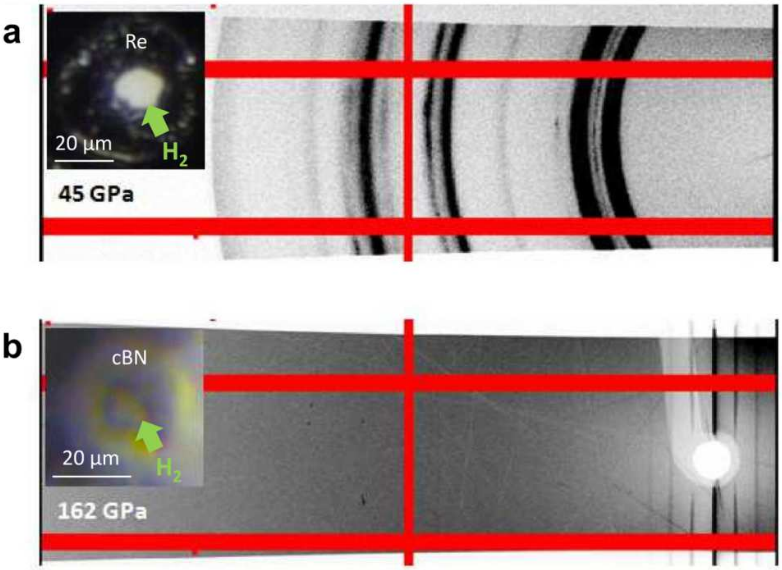

Extended Data Fig. 1

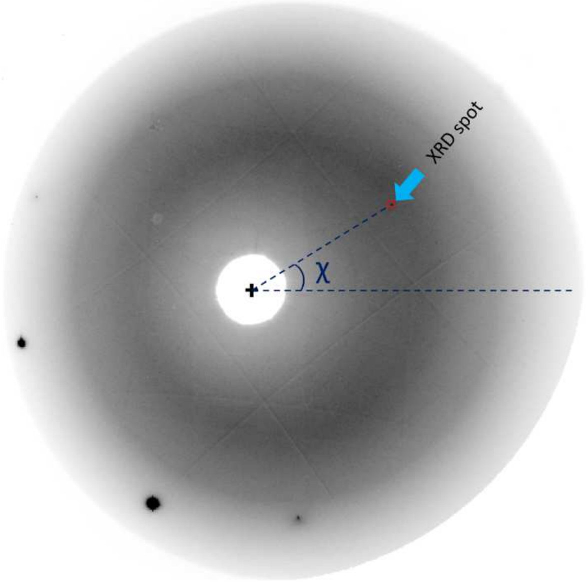

Extended Data Fig. 2

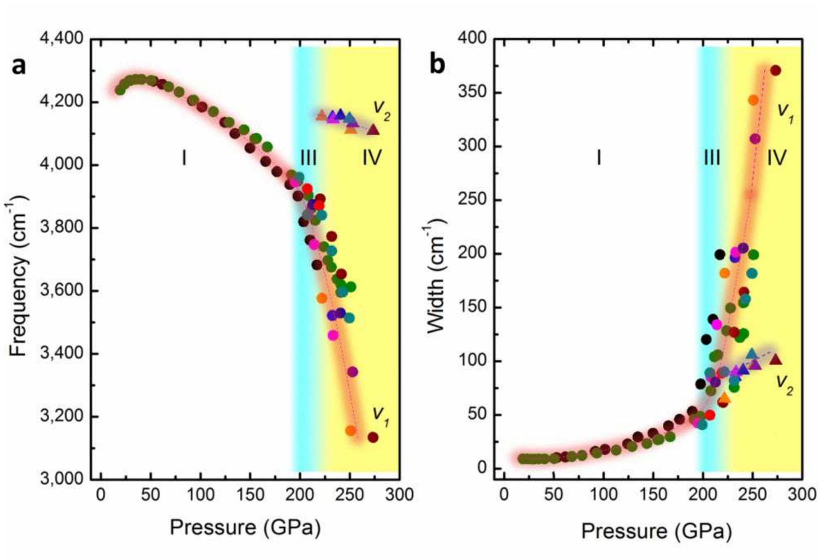

595
596 **Extended Data Fig. 3**

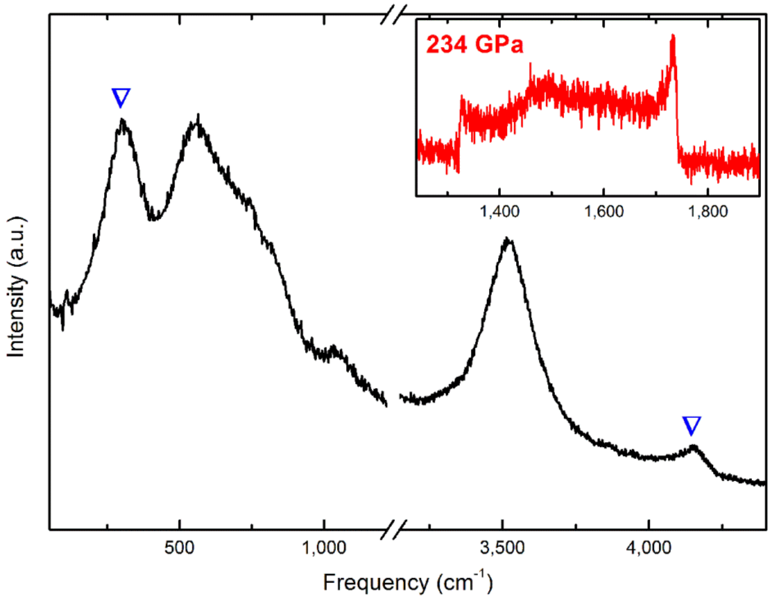

Extended Data Fig. 4

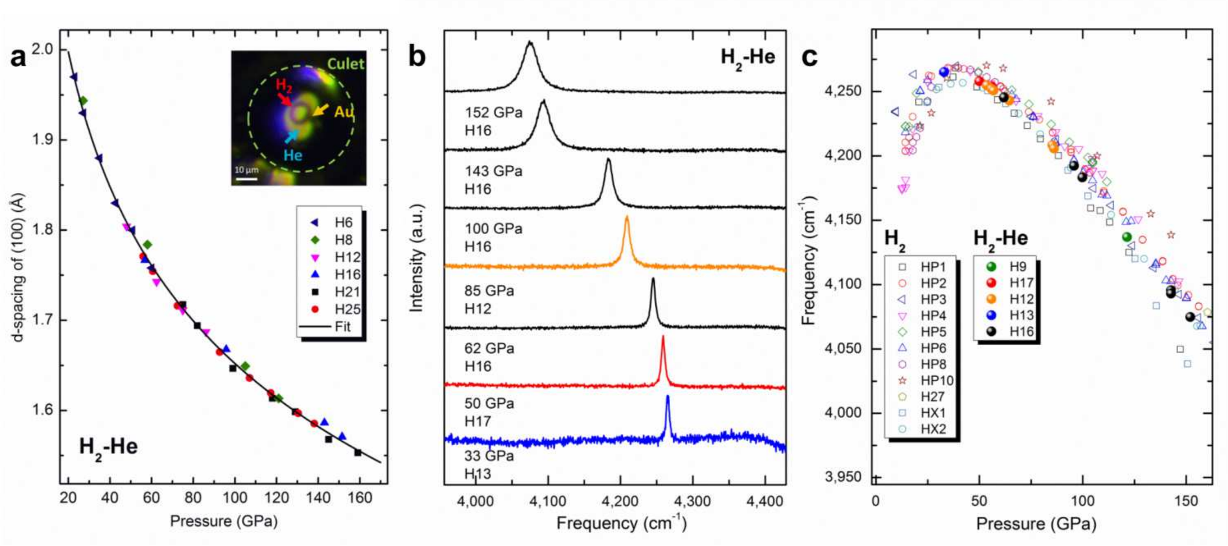

Extended Data Fig. 5

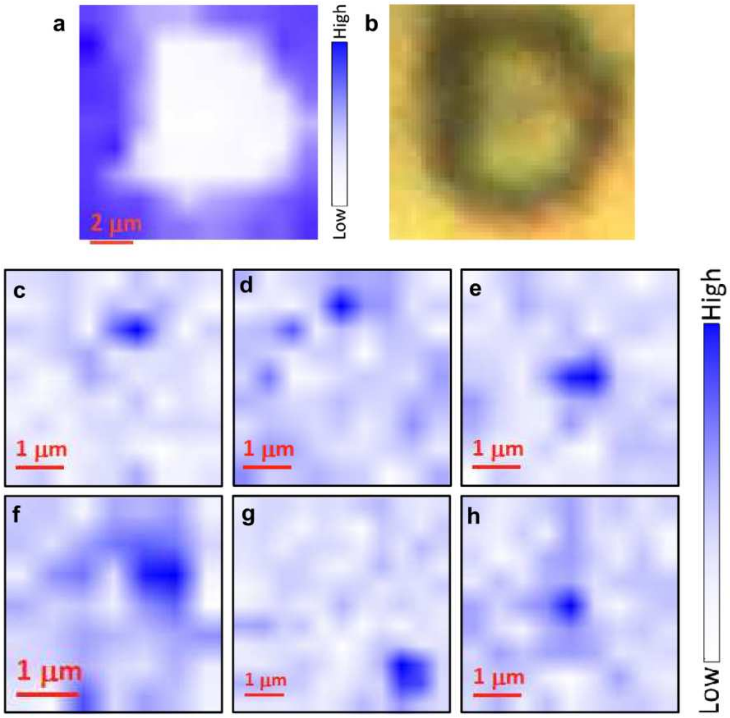

Extended Data Fig. 6

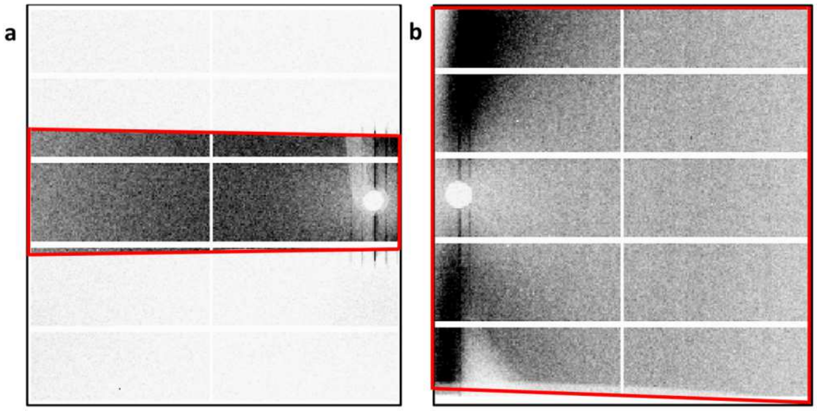

Extended Data Fig. 7

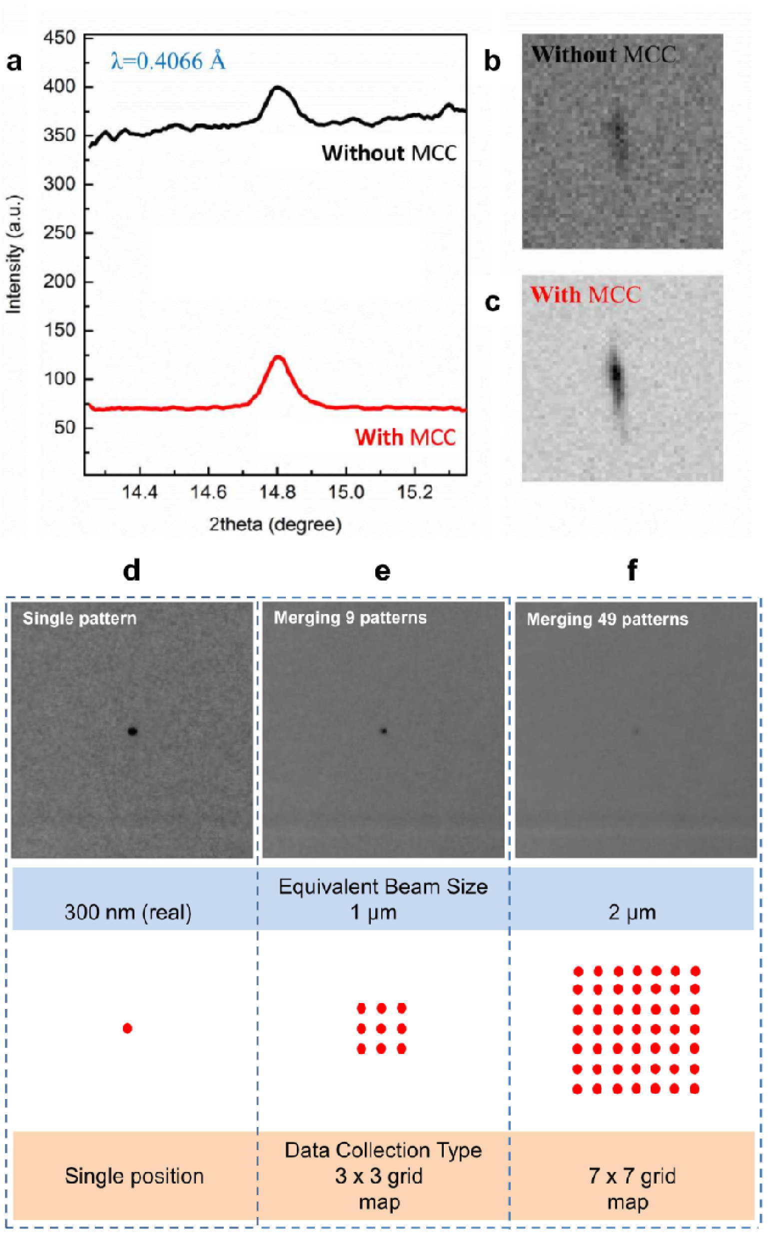

Extended Data Fig. 8

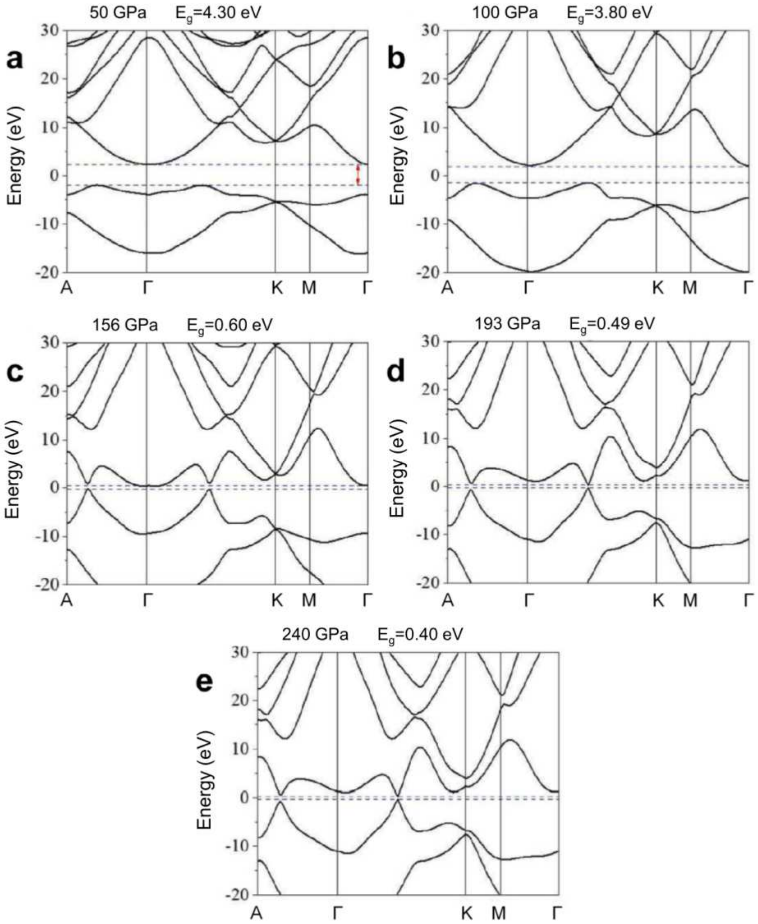

607
608 **Extended Data Fig. 9**

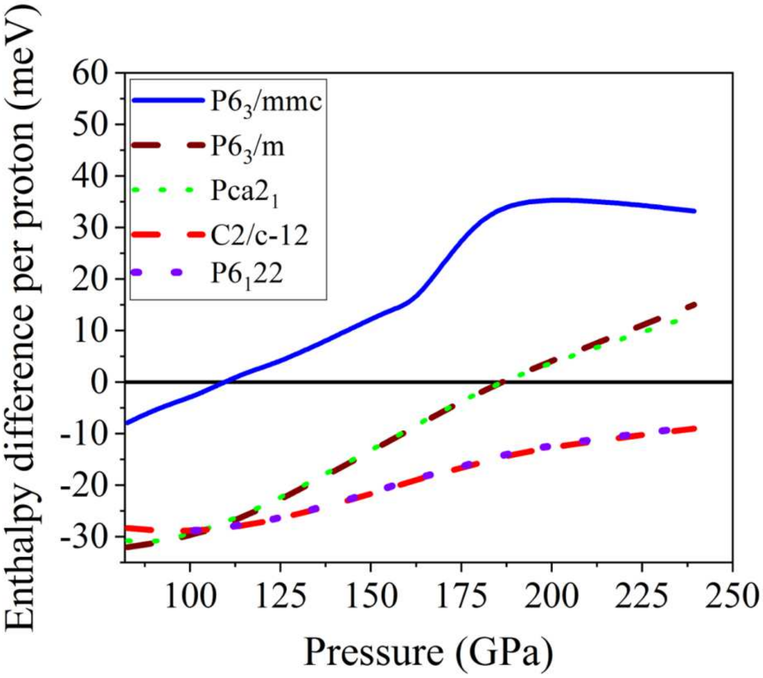

Extended Data Fig. 10

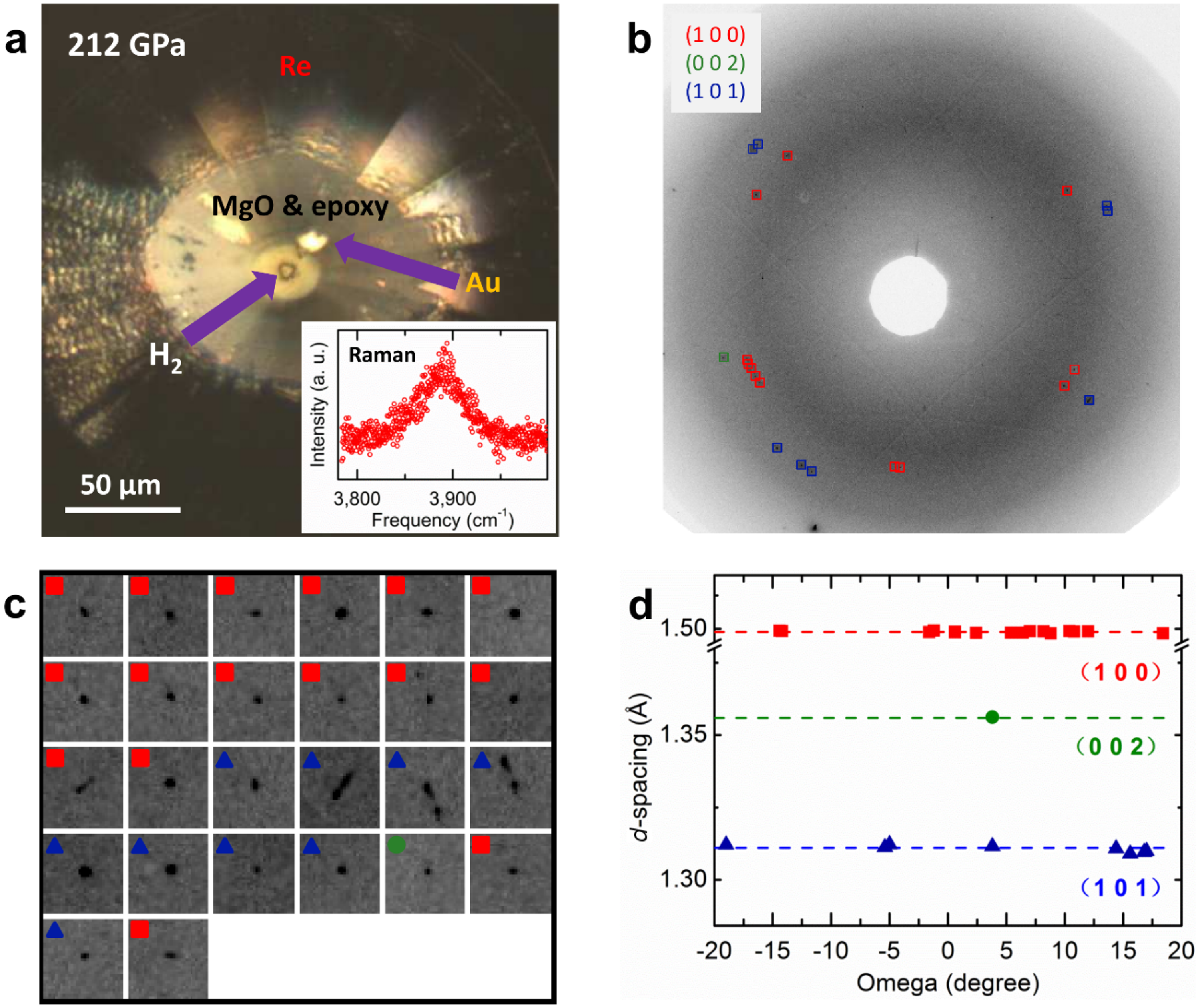
a
212 GPa
Re
MgO & epoxy
Au
H_2
50 μm
Raman
Intensity (a. u.)
3,800
3,900
Frequency (cm^{-1})
b
(1 0 0)
(0 0 2)
(1 0 1)
c
d
1.50
1.35
1.30
d-spacing (Å)
(1 0 0)
(0 0 2)
(1 0 1)
-20
-15
-10
-5
0
5
10
15
20
Omega (degree)

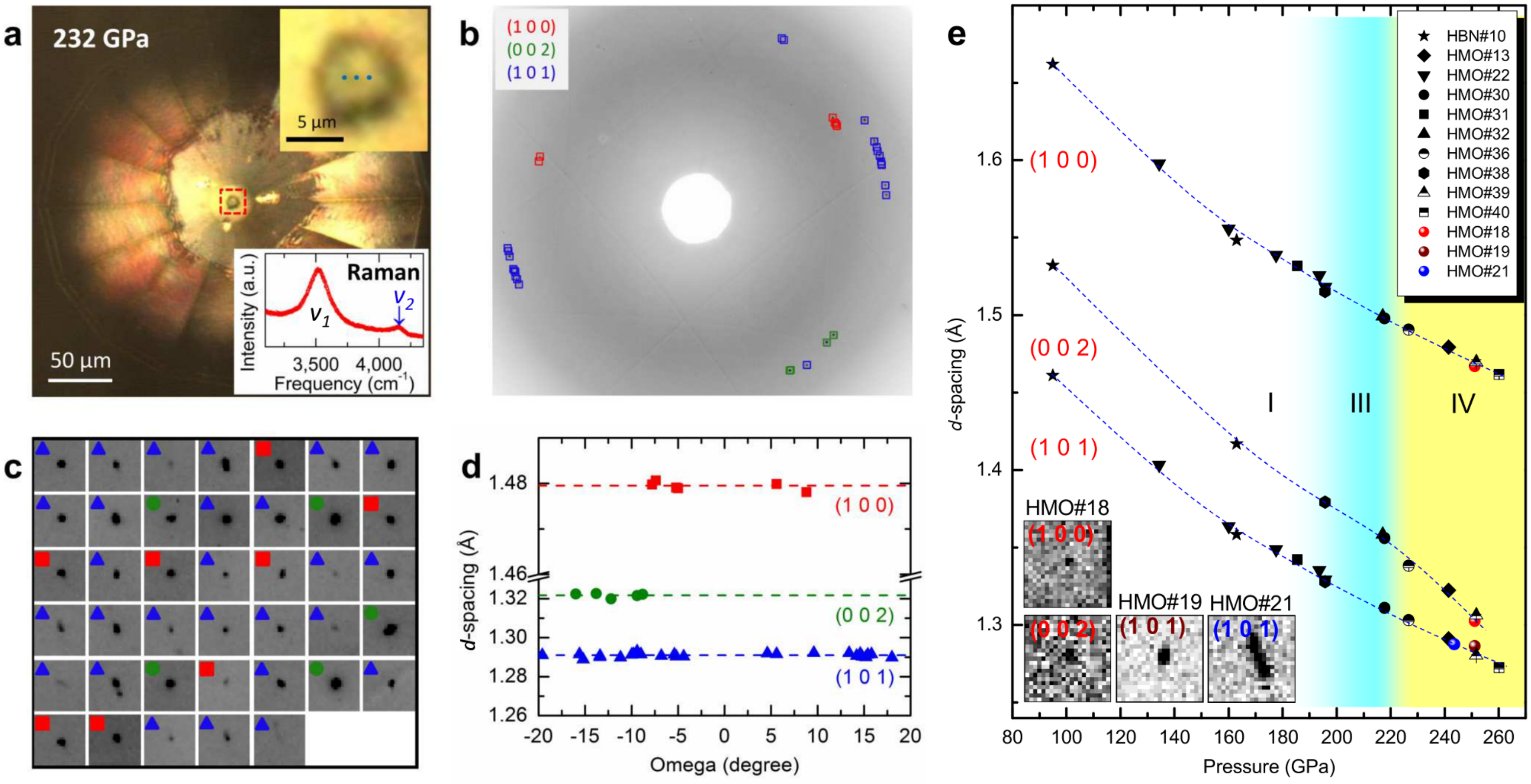
a
232 GPa
5 μm
50 μm
Raman
Intensity (a.u.)
v_1
v_2
3,500
4,000
Frequency (cm^{-1})
b
(1 0 0)
(0 0 2)
(1 0 1)
c
d
d-spacing (Å)
1.48
1.46
1.32
1.30
1.28
1.26
(1 0 0)
(0 0 2)
(1 0 1)
-20
-15
-10
-5
0
5
10
15
20
Omega (degree)
e
HBN#10
HMO#13
HMO#22
HMO#30
HMO#31
HMO#32
HMO#36
HMO#38
HMO#39
HMO#40
HMO#18
HMO#19
HMO#21
d-spacing (Å)
1.6
1.5
1.4
1.3
(1 0 0)
(0 0 2)
(1 0 1)
I
III
IV
HMO#18
(1 0 0)
(0 0 2)
HMO#19
(1 0 1)
HMO#21
(1 0 1)
80
100
120
140
160
180
200
220
240
260
Pressure (GPa)

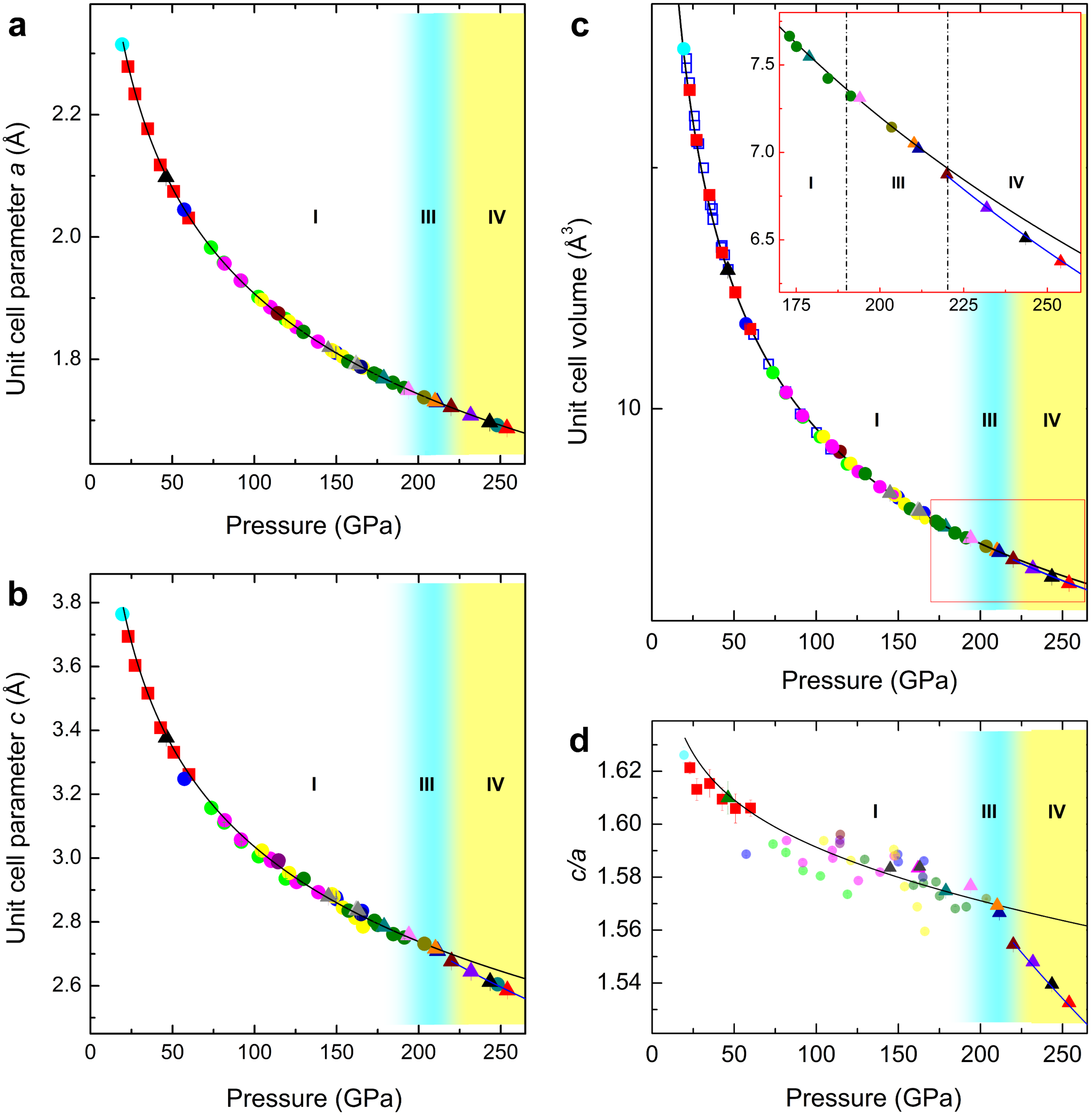
a
Unit cell parameter a (Å)
2.2
2.0
1.8
Pressure (GPa)
0
50
100
150
200
250
I
III
IV
b
Unit cell parameter c (Å)
3.8
3.6
3.4
3.2
3.0
2.8
2.6
Pressure (GPa)
0
50
100
150
200
250
I
III
IV
c
Unit cell volume (Å^3)
10
Pressure (GPa)
0
50
100
150
200
250
I
III
IV
7.5
7.0
6.5
175
200
225
250
I
III
IV
d
c/a
1.62
1.60
1.58
1.56
1.54
Pressure (GPa)
0
50
100
150
200
250
I
III
IV